



Hollow block masonry wall reinforced by built-in structural configuration: Seismic behavior analysis



Xiaojie Zhou^{a,b,*}, Jinpeng Du^{a,b}, Quanmin Peng^{a,b}, Peiqi Chen^{a,b,*}

^a Tianjin Key Laboratory of Civil Buildings Protection and Reinforcement, Tianjin, 300384, China

^b School of Civil Engineering, Tianjin Chengjian University, Tianjin, 300384, China

ARTICLE INFO

Keywords:

Hollow-block masonry wall
Built-in structural scheme
Horizontal low cycle loading test
Seismic performance
Finite element analysis

ABSTRACT

This paper proposes a new type of wall with built-in structural configuration. Common blocks with single-row holes serve as grouted recesses in the construction of built-in structural columns, core columns, and diagonal braces of the wall. The construction of this built-in structural scheme is more efficient and cost-effective than normal wall structures because it necessitates no formwork or large construction equipment. A nonlinear finite element analysis and integral modeling process were conducted based on horizontal cyclic loading tests of four hollow-block masonry walls with different built-in structural schemes. The feasibility of the model was verified by comparing the test and calculation results. The effects of different structural schemes on the failure process, failure mode, bearing capacity, stiffness degradation, and displacement ductility of the masonry wall were analyzed to determine the optimal structural details. The built-in structural columns and core columns should be concentrated at both wall ends while core columns are added in the center of the wall as necessary; a horizontal steel tie mesh can ensure cooperative bonding among structural columns and core columns. The effects of various strength grades of grouted concrete on masonry wall seismic performance with the optimized scheme were also observed.

1. Introduction

The construction of masonry walls is more efficient with hollow blocks than solid clay blocks due to their larger size. Certain types of hollow block are also particularly environmentally friendly and cost-effective because they can be manufactured from industrial waste residue [12]. Hollow blocks are widely used in building projects as load-bearing or non-load-bearing walls.

Unreinforced hollow-block masonry buildings must be carefully designed for seismic performance; the structures are highly vulnerable to earthquakes because of their low tensile and shear strength, the poor ductility of unreinforced hollow-block masonry (URHM), and other issues. However, the in-plane shear capacity of unreinforced masonry shear walls does not increase as bond strength increases [3]. Many researchers have proposed strengthening techniques to retrofit URHM. Existing strengthening schemes can be divided into two main categories: reinforced hollow-block masonry (RHM) and external or internal strengthening with fiber reinforced polymer (FRP) [4,5] with posttensioned steel, FRP bars [6-8], or other materials [9-11]. The former, an internal strengthening method, is normally used for new masonry structures; the latter, an external strengthening method, is

normally used to strengthen or repair existing structures. The main disadvantage of the latter includes the toxicity and poor fire resistance of bonding materials as well as the complexity and high cost of post-tensioning construction.

RHM, in which horizontal and vertical reinforcement bars are embedded, is more commonly adopted than external or internal strengthening methods in masonry construction projects worldwide. Three methods of embedment are available, as shown in Fig. 1. In the first method, the URHM is built first followed by filling selected hollow cores with reinforced grout containing a single reinforcing bar and no shear ties to form core columns [12-14] (Fig. 1(a)). In this paper, this type of RHM is referred to as “partially grouted masonry” (PGM). In the second method, structures consist of load-bearing masonry walls and confining elements at the wall perimeter. These confining elements are generally reinforced concrete (RC) tie-beams and tie-columns which include several longitudinal bars and shear ties, respectively [15-17] (Fig. 1(b)). This type of RHM is generally referred to as “confined masonry” (CM).

In the third method (Fig. 1(c)), the cross section of masonry walls is T-shaped and consists of rectangular wall and boundary elements located at ends of the wall. All rectangular wall and boundary elements

* Corresponding authors. School of Civil Engineering, Tianjin Chengjian University, Tianjin, 300384, China.

E-mail addresses: zhouxj88888@126.com (X. Zhou), cpq@tcu.edu.cn (P. Chen).

<https://doi.org/10.1016/j.soildyn.2019.105815>

Received 15 April 2019; Received in revised form 15 July 2019; Accepted 12 August 2019

Available online 28 August 2019

0267-7261/© 2019 The Authors. Published by Elsevier Ltd. This is an open access article under the CC BY-NC-ND license

(<http://creativecommons.org/licenses/by-nc-nd/4.0/>).

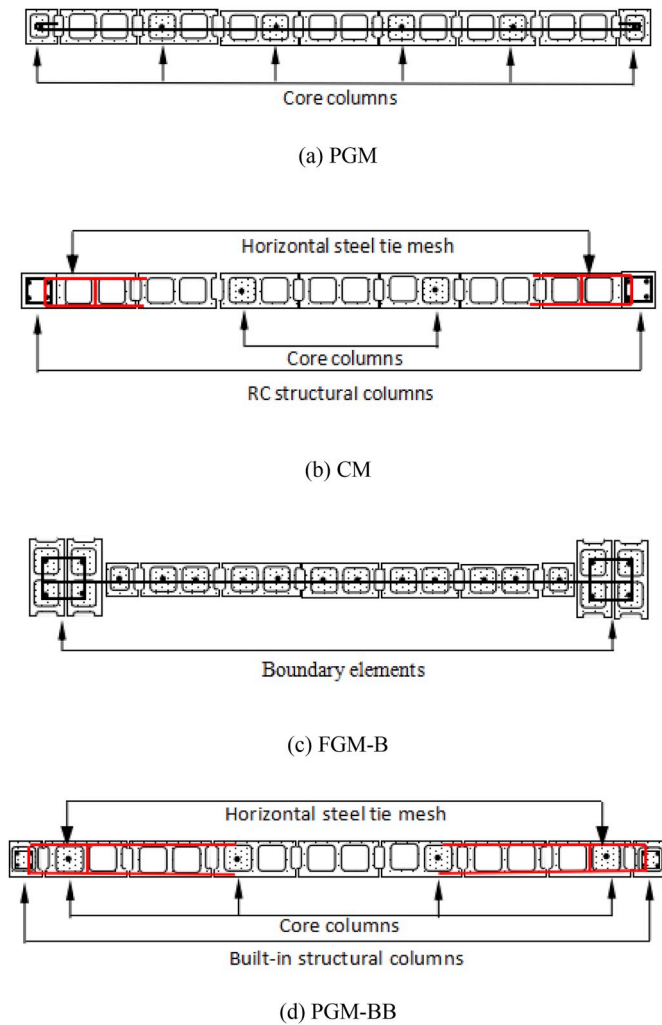


Fig. 1. Four reinforced hollow-block masonry walls.

are built with hollow blocks. The rectangular wall part is usually constructed with a single-leg horizontal reinforcement and a single layer of vertical reinforcement, while all hollow cores are grouted with reinforced grout. Closed ties and multiple layers of vertical bars form the boundary elements thus providing a confining reinforcement cage. This type of wall is stronger and more ductile with less strength degradation than walls prepared by the two methods discussed above; it is preferred for reinforced concrete masonry shear walls in multi-to-high-rise buildings [18, 19]. This kind of RHM is referred to in this paper as “fully grouted masonry with boundary elements” (FGM-B). Compared to FGM-B, PGM and CM are usually used for load-bearing walls in ordinary masonry structures. PGM is representative of indirect confinement and CM of direct confinement [14]. Direct confinement is more effective than indirect confinement in hollow concrete masonry unit shells. However, indirect grout confinement can be constructed more quickly (without formwork) and hence may be more cost-effective [5].

As per the advantages of PGM, CM, and FGM-B [20], a new reinforced hollow block masonry wall configuration based on the common single-row hollow block is proposed in this paper. This type of RHM is termed “partially grouted masonry with built-in boundary elements” (i.e., built-in structural columns) reinforced with closed ties and multiple layers of vertical bars, abbreviated as PGM-BB, as shown in Fig. 1(d). In PGM-BB walls, the block itself serves as a grouted recess to construct a built-in structural column, built-in core column, and built-in diagonal bracing. The reinforced masonry structure with PGM-BB can be constructed conveniently and cost-effectively enough for application in one-to-low rise masonry buildings in rural areas.

There are mutual effects among in-plane and out-of-plane responses of masonry walls [21]; this paper discusses only an experiment and nonlinear finite element analysis which were conducted to observe the in-plane seismic performance of PGM-BB walls due to space limitations. Horizontal cyclic loading tests of four hollow-block masonry walls with different built-in structural schemes were first conducted, then integral finite element models were established in ABAQUS software [8–10,22]. The feasibility of the modeling method was verified. Next, the mechanical behaviors and seismic performance of different structural schemes were compared to determine the optimal structural details of the wall. The effects of different strength grades of poured concrete on the seismic performance of the optimized wall were also investigated.

2. Experimental program

2.1. Specimen design and fabrication

Four hollow-block walls were designed and fabricated. The structural characteristics of the specimens are described in Table 1; the size and structural layout of the specimens are shown in Fig. 2. In specimen ZW-1, the built-in structural columns and core columns were concentrated at the both ends of the wall. In specimen ZW-2, the built-in structural columns and core columns were in a dispersed layout scheme. In specimen XCW-1, the built-in structural column was associated with a built-in diagonal brace. The upper and lower ends of the built-in structural columns, core columns, and diagonal braces were connected with a top beam and bottom beam, respectively.

The diagonal brace must be suited to the size of the diagonal bracing channel formed by the U-shaped hollow-blocks and corresponding polystyrene wedge block (PWB), as shown in Fig. 3. The size of the main block of the wall in this setup is 395 mm × 190 mm × 190 mm, the auxiliary block is 190 mm × 190 mm × 190 mm, and the U-shaped block used in the top beam and the built-in diagonal brace is 190 mm × 190 mm × 190 mm. A block of strength grade MU7.5 and masonry mortar of strength grade Mb7.5 were used. The cross-section size of the built-in structural column and core column is 130 mm × 130 mm and the cross-section size of the diagonal brace is 135 mm × 130 mm. The longitudinal bars of the built-in structural column, core column with diagonal brace, and top beam are 4Φ8, 1Φ8, and 4Φ12, respectively. All stirrups in the built-in structural column and the top beam are Φ6@100.

During construction of the wall, horizontal steel tie meshes were embedded along the height of the wall every two-course, as shown in Fig. 2. In specimen ZW-1, one end of the steel mesh extends to the built-

Table 1
Specimen design conditions.

Specimen number	Built-in structural column	Core column	Diagonal brace	Wall configuration
PW	–	–	–	
ZW-1	Built-in at both ends of the wall	Built-in and close to the structural column	–	
ZW-2	Built-in at both ends of the wall	Built-in along the trisection of the wall	–	
XCW-1	Built-in at both ends of the wall	–	Built-in	

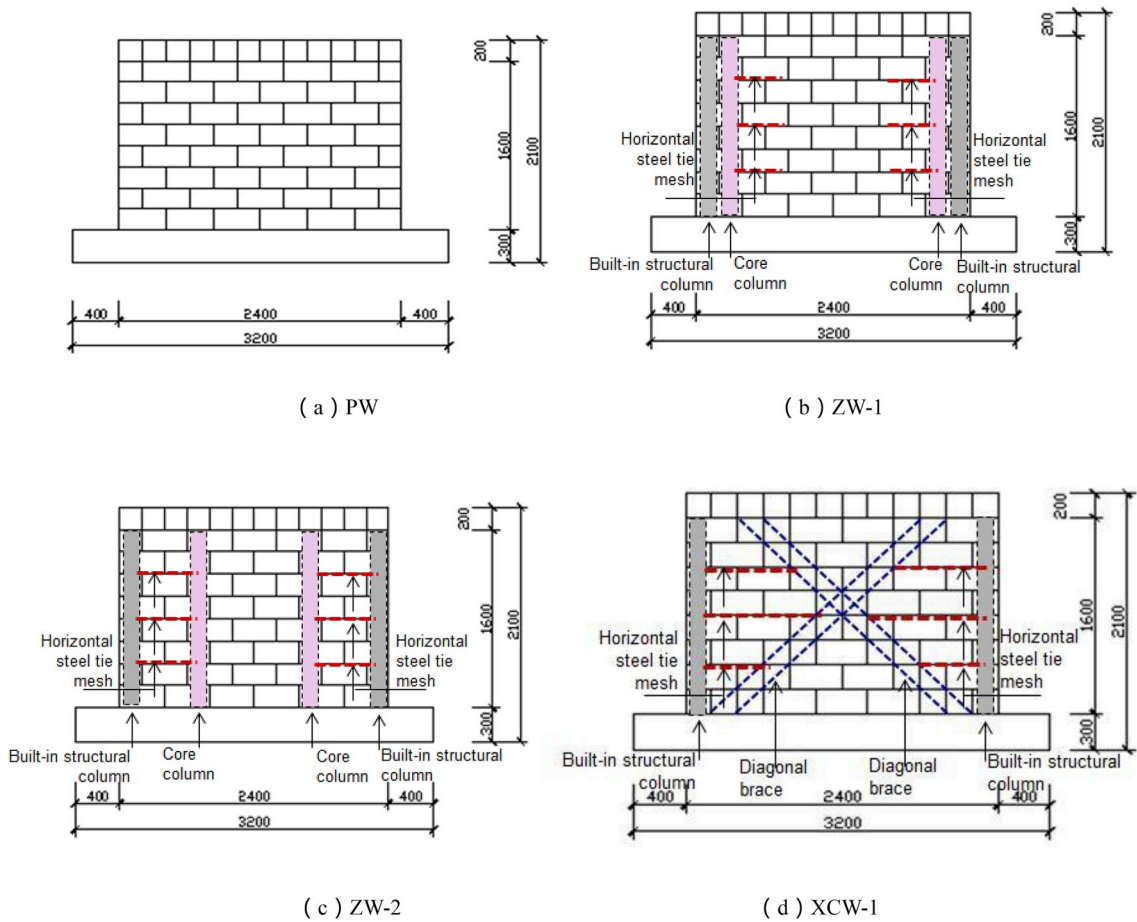


Fig. 2. Size and structural layout of the specimens.

in structural column and the core column while the other end extends into the wall not less than 500 mm away. In specimens ZW-2 and XCW-1, one end of the steel mesh extends into the built-in structural column set at each end of the wall; the other end extends into the core column or diagonal brace to form an effective tie. The specimens under construction are shown in Fig. 4.

2.2. Test setup and loading system

To simulate the mechanical state of the wall under an earthquake, the bottom of the wall should be fixed while the top is able to translate. The test setup used in this study is shown in Fig. 5. Cyclic lateral load was applied at the end of the top beam by an electro-hydraulic actuator. Axial force was applied up to the desired value and kept constant at the 1/4 point of the top beam by two hydraulic jacks. For free lateral movement during cyclic loading, low friction sliding plates were placed

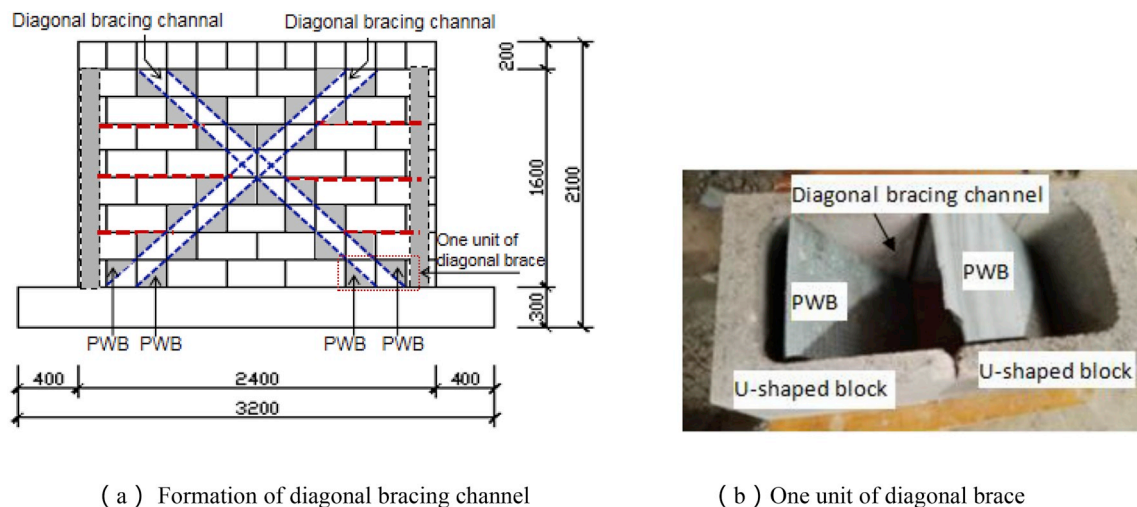


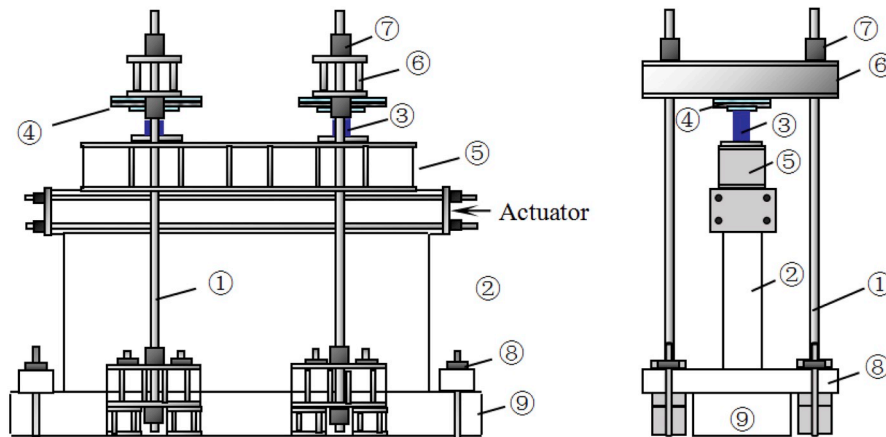
Fig. 3. Diagonal bracing channel.



(a) Built-in structural column reinforcement

(b) Diagonal brace making

Fig. 4. Specimens under construction.



Notes: ① Vertical loading device; ② Wall; ③ Jack; ④ Low friction sliding plate;
 ⑤ Steel beam; ⑥ Steel crossbeam; ⑦ Bolt; ⑧ Pressure beam;
 ⑨ Base of the wall

(a) Schematic diagram of loading device



(b) Photo of loading device

Fig. 5. Loading device.

on the jacks. The lateral loading history is shown in Fig. 6. The vertical load applied on the wall was 160 kN and the vertical compressive stress of the wall is almost 0.35 MPa. Before cracking of the specimen (drift ratio about 1/2000), one fully reversed loading cycle was applied at each displacement amplitude level. Three cycles were applied after cracking. Failure was assumed to occur when the strength of the specimen was reduced by more than 15% of the peak strength.

During the test, the position of the first crack, the crack

development process, and the final distribution of cracks upon damage to the specimen were observed. The top displacement of the wall was observed in each loading and unloading process. Five gauges were arranged evenly along the length direction of each longitudinal bar of the built-in structural column, core column, and diagonal brace to monitor the strain of the steel bar during the tests.

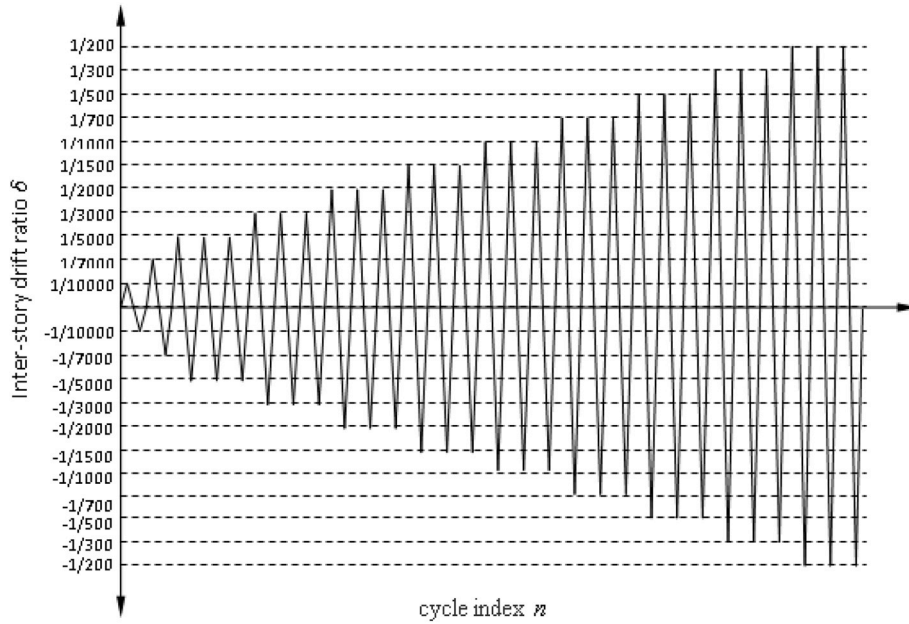


Fig. 6. Lateral loading history.

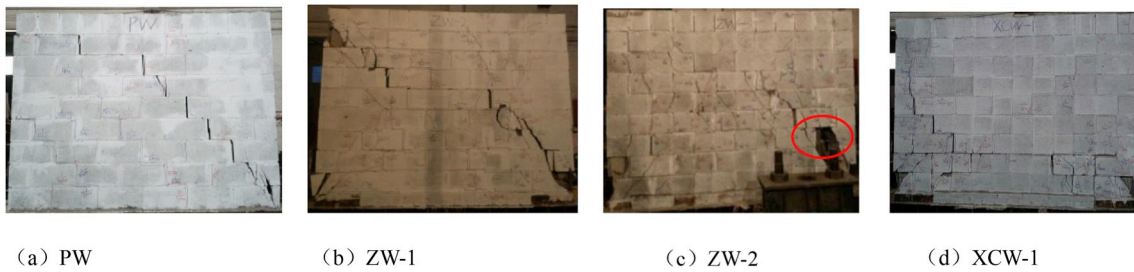


Fig. 7. Specimen failure modes.

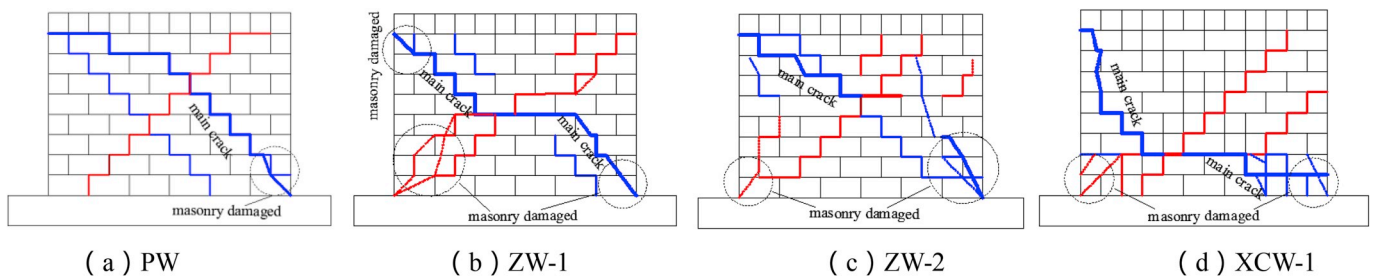


Fig. 8. Final crack distributions of specimens.

Table 2
Test results.

Specimen number	Crack		Peak		Failure		K_e /kN.mm ⁻¹	μ
	P_{cr} /kN	Δ_{cr} /mm	P_{max} /kN	Δ_{max} /mm	P_u /kN	Δ_u /mm		
PW	33.86	0.45	98.16	0.94	83.43	1.27	75.24	2.82
ZW-1	91.01	0.69	151.69	6.73	128.94	9.13	131.90	13.23
ZW-2	95.06	0.95	175.93	8.14	149.54	11.15	100.06	11.74
XCW-1	93.91	0.91	174.03	5.17	147.93	7.69	103.20	8.45

* P_{cr} , P_{max} , P_u : loads of specimens corresponding to cracking point, peak point, and failure point, respectively; Δ_{cr} , Δ_{max} , Δ_u : displacements of specimens corresponding to cracking point, peak point, and failure point, respectively; K_e : equivalent initial stiffness of wall, $K_e = P_{cr}/\Delta_{cr}$; μ : displacement ductility, $\mu = \Delta_u/\Delta_{cr}$.

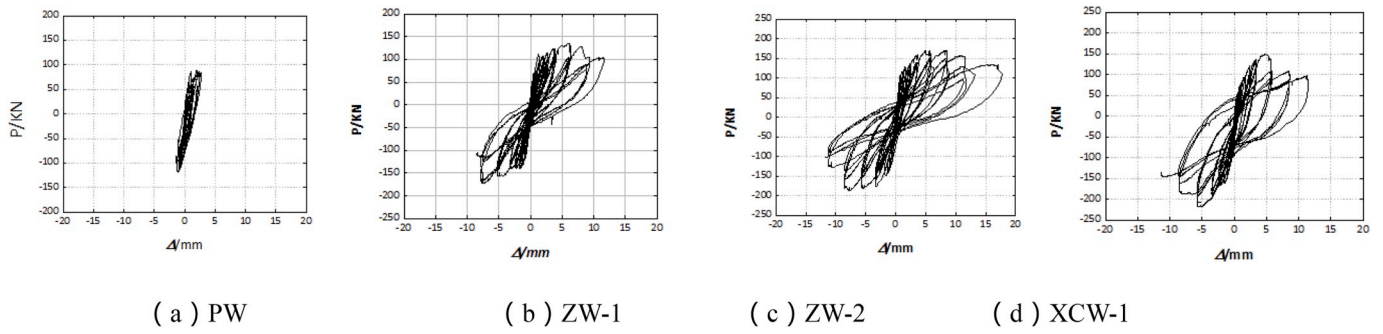


Fig. 9. Hysteretic curves.

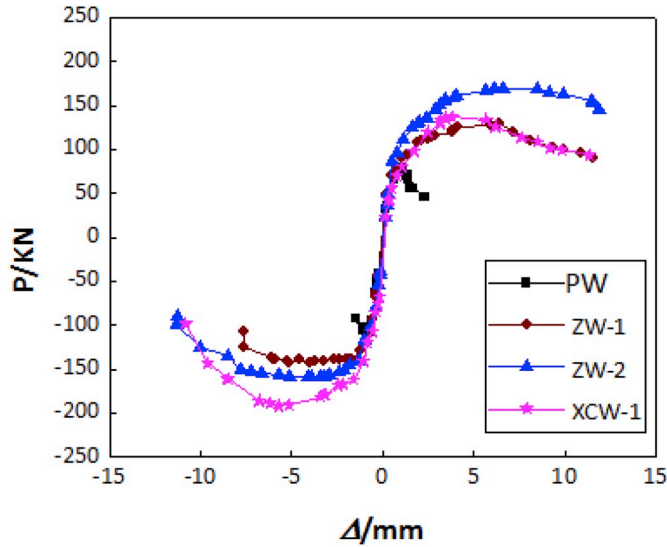


Fig. 10. Force-displacement skeleton curve.

2.3. Experimental results

2.3.1. Failure mode

The final failure modes of the specimens are shown in Fig. 7 and the final crack distributions are shown in Fig. 8.

When the test ended, specimen PW was split into two parts along the diagonal or stepped main crack indicative of brittle characteristics. The built-in structural column and core column restrained the wall and ameliorated the brittleness. For specimen ZW-1, the built-in structural column and core column arranged at the ends of the wall formed a composite section with relatively large size and stiffness. The top beam and combined structural column and core column component formed a similar framework which restrained the intermediate wall effectively.

Specimen ZW-2 showed structural uniformity as the horizontal steel tie bonded the structural columns and core columns dispersedly arranged in the wall. The restraining effect on the wall was further enhanced by this design scheme, as was the bearing capacity, ductility, and energy consumption.

When specimens ZW-1 and ZW-2 failed, the built-in structural column and core column presented inclined cracks or shear failure along the direction of stepped main crack of the wall. To this effect, the built-in structural column and core column played important roles in the performance of the wall as a whole. The cracks were more fully

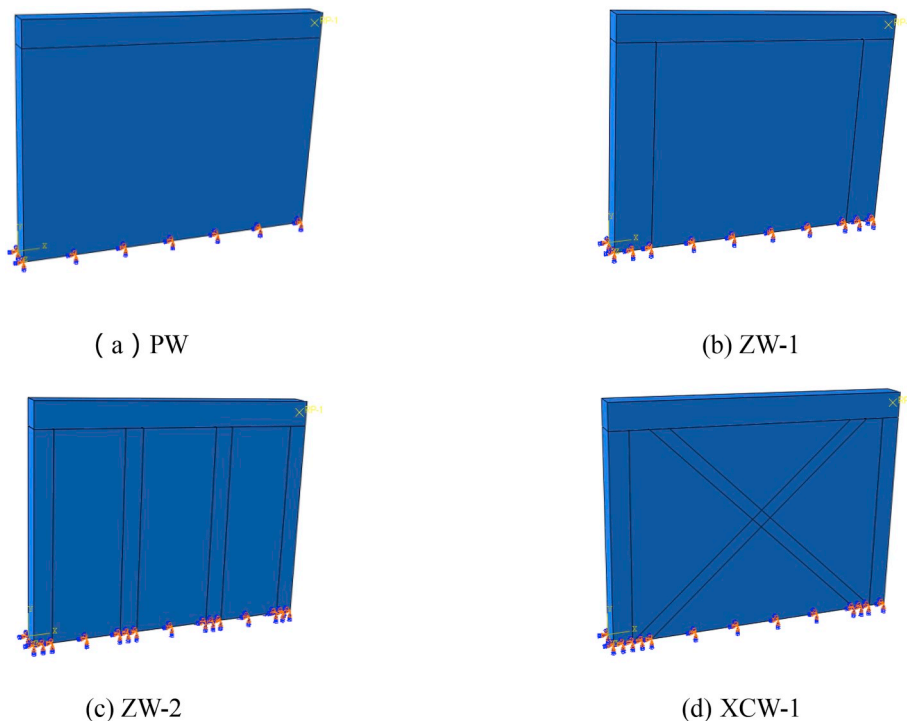


Fig. 11. Finite element models.

Table 3
Material strength parameters.

Type	Masonry	Longitudinal reinforcement ($\phi 8$)	Stirrup ($\phi 6$)	Mortar	Filled hollow block masonry	Top beam
Compression strength (MPa)	4.818	386.8	336.3	6.02	9.21	11
Tensile strength (MPa)	–	386.8	336.3	0.602	1.57	1.89

Table 4
Material elastic parameters.

Type	Masonry	Longitudinal reinforcement ($\phi 8$)	Stirrup ($\phi 6$)	Mortar	Filled hollow block masonry	Top beam
Elastic modulus (MPa)	2409	2.1×10^5	2.3×10^5	4774	4607	5567
Poisson ratio	0.2	0.3	0.3	0.24	0.2	0.2

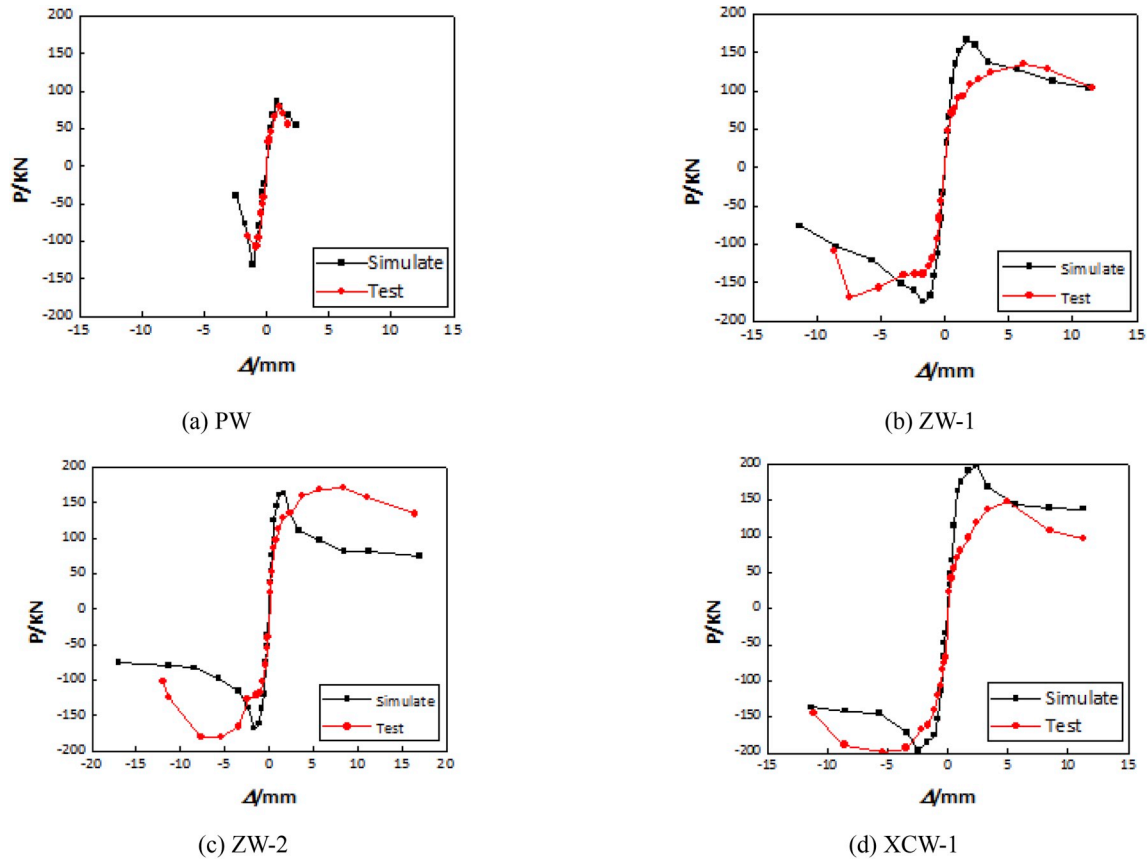


Fig. 12. Load-displacement skeleton curves between simulation and test results.

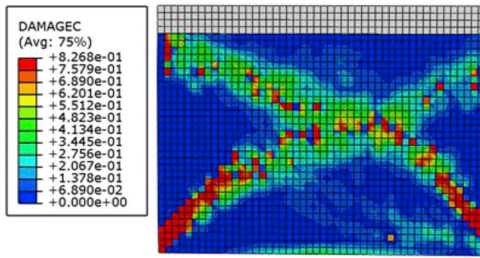
Table 5
Simulation results.

Specimen number	Crack		Peak		Failure		$K_e/kN.mm^{-1}$	μ
	F_{cr}/kN	Δ_{cr}/mm	P_{max}/kN	Δ_{max}/mm	P_u/kN	Δ_u/mm		
PW	58.35	0.51	107.33	1.13	91.23	1.41	114.41	2.76
ZW-1	92.12	0.57	175.12	1.70	148.85	2.73	161.61	4.79
ZW-2	95.44	0.67	168.35	2.11	142.56	2.53	141.79	3.78
XCW-1	114.65	0.80	192.48	2.39	167.25	3.11	143.32	3.89

developed and evenly distributed in ZW-2, where the local masonry between the right core column and structural column was seriously damaged and a cavity appeared in the wall (Fig. 7(c)). In effect, the ends of the wall are crucial to the wall's working performance and should be strengthened appropriately.

The built-in diagonal braces bore tensile and compressive stress

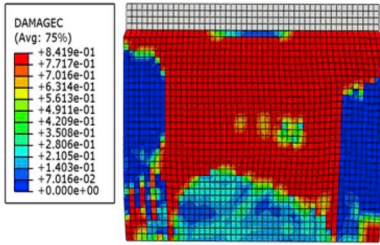
during the loading process in specimen XCW-1, which improved the horizontal bearing capacity of the wall. When XCW-1 failed, the upper part of the wall was almost intact. However, the roots of the two diagonal braces and the surrounding masonry were severely damaged; the roots of the built-in structural column presented shear cracks. Part of the horizontal steel tie mesh between the structural column and



(a) Final compression damage of PW



(b) Test failure of PW



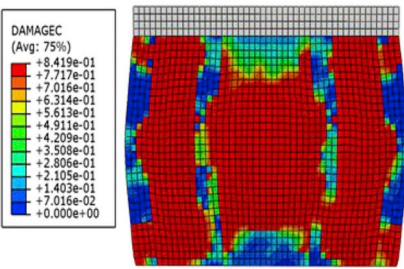
(c) Final compression damage of ZW-1



(d) Test failure of ZW-1



(e) Failure of built-in structural column and core column in ZW-1



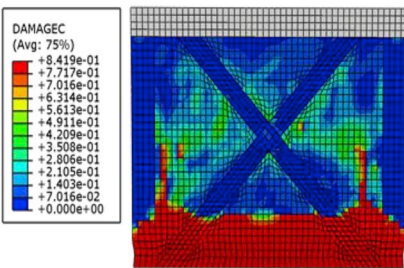
(f) Final compression damage of ZW-2



(g) Test failure of ZW-2



(h) Failure of built-in structural column and core column in ZW-2



(i) Final compression damage of XCW-1



(j) Test failure of XCW-1



(k) Failure of built-in structural column and diagonal brace in XCW-1

Fig. 13. Final compression damage distribution (simulated) and failure mode (tested).

diagonal brace was broken, indicating that the tie mesh is advantageous to cooperation between the structural column and diagonal brace.

2.3.2. Experimental results and analysis

The test results are listed in Table 2. Hysteretic curves and force-displacement skeleton curves of the specimens are shown in Fig. 9 and Fig. 10.

As shown in Fig. 9, the hysteretic loop of ZW-1 formed an inverted S-shape while the hysteretic loops of ZW-2 and XCW-1 formed arch shapes. In other words, the energy dissipation ability of the latter two is better. Table 2 shows that the cracking load of the wall increased by about 175.6% on average with the setting of the built-in structural column, core column, or diagonal brace. The peak load of the wall also

increased due to the setting of the built-in structural column, core column, or diagonal brace. Compared to specimen PW, the peak load of ZW-1 increased by about 54.5%; ZW-2 was approximately equal to XCW-1 at an increase of about 78.3%. Thus, a dispersed structural column and core column layout, or a structural column with a built-in diagonal brace, appears to be more advantageous in terms of bearing capacity.

The equivalent initial stiffness of the wall increased after setting a built-in structural column, core column, or diagonal brace. Compared to specimen PW, ZW-1 increased by about 75.3% and ZW-2 was again similar to XCW-1 with an increase of about 35.1%. In regards to equivalent initial stiffness, it is advantageous to construct a concentrated built-in structural column and core column layout.

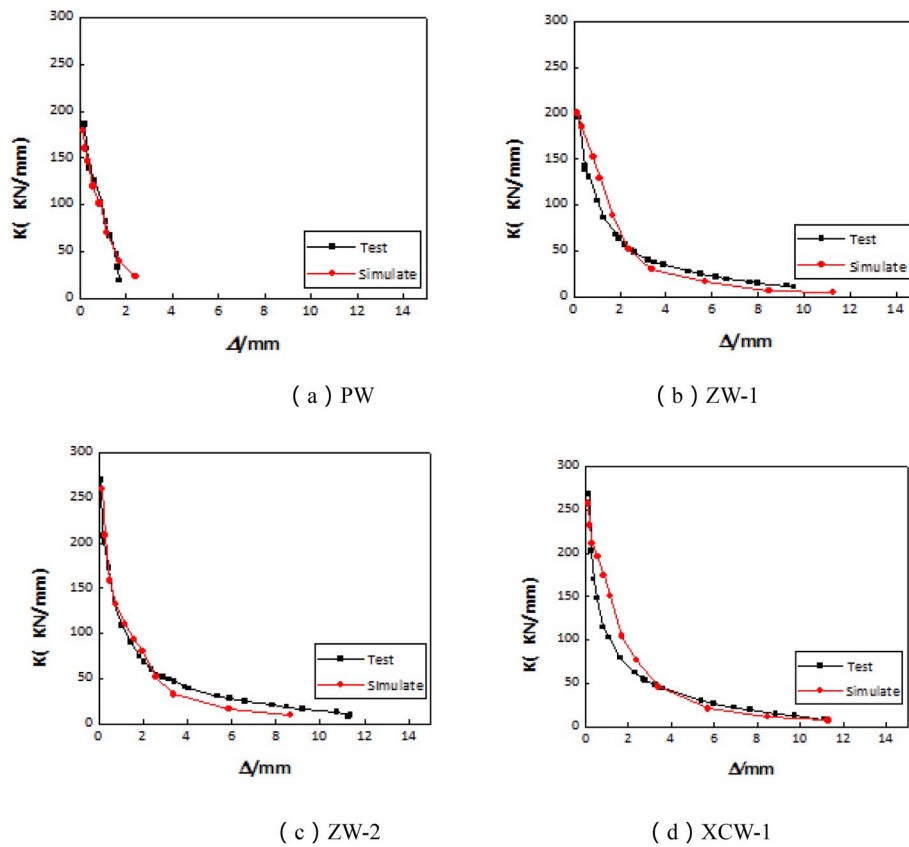


Fig. 14. Stiffness degradation curves.

Table 6
Added specimens.

Specimen number	Built-in structural column	Core column	Diagonal brace	Wall configuration
ZW-3	Built-in at both ends of the wall	-	-	
ZW-4	Built-in at both ends of the wall	Built-in and close to the structural column, and in the center of the wall	-	

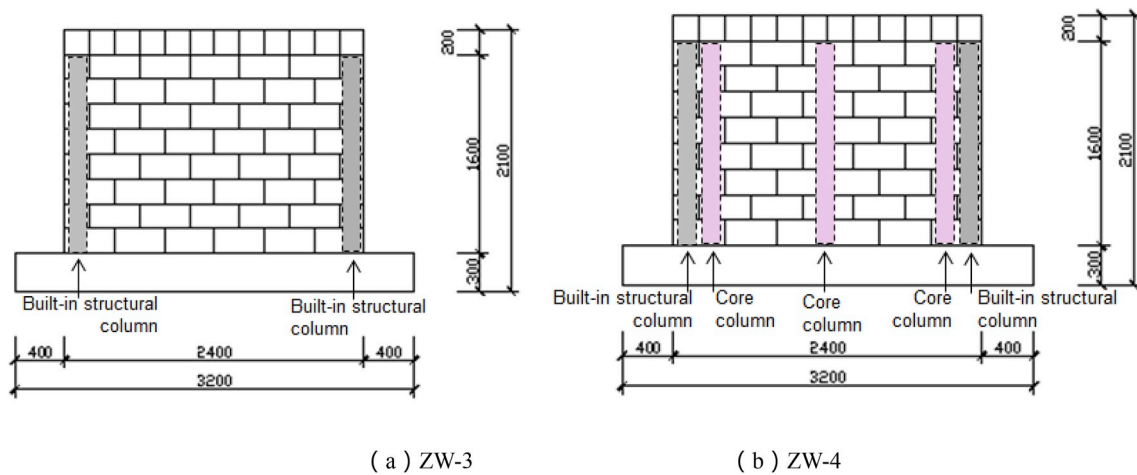


Fig. 15. Dimension and structural layout of added specimens.

The displacement ductility of the wall also increased after setting the built-in structural column, core column, or diagonal brace. Compared to specimen PW, the displacement ductility of ZW-1, ZW-2, and XCW-1 increased by 369.1%, 316.3%, and 199.6%, respectively.

The concentrated built-in structural and core column layout was optimal as far as the displacement ductility of the wall. The dispersed structural column and core column layout increased the peak load to the same extent as the wall with the built-in diagonal brace, but the

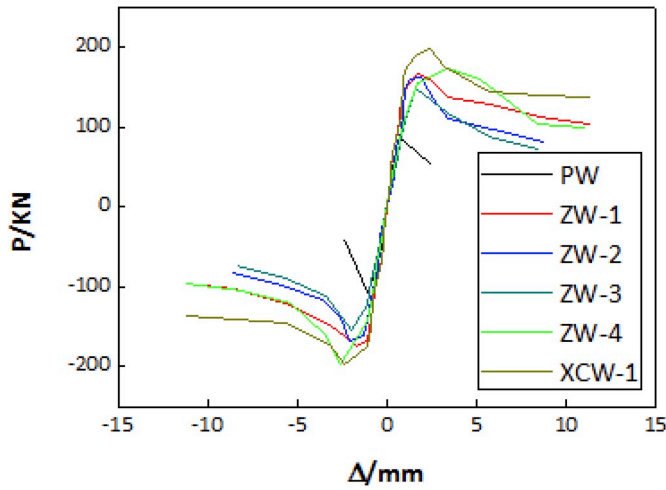


Fig. 16. Load-displacement skeleton curves.

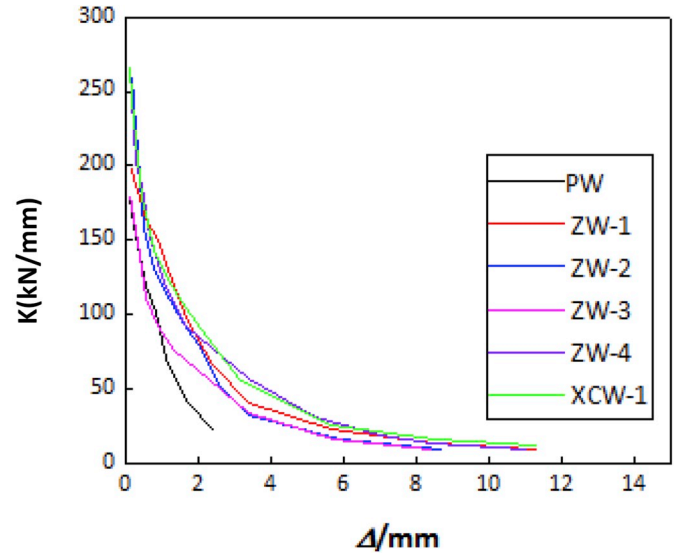


Fig. 17. Stiffness degradation curves.

former resulted in better ductility.

3. Finite element model verification

3.1. Model establishment

Integral finite element models of the walls with the built-in structure schemes discussed above were established in ABAQUS software (Fig. 11). The rationality of the model was verified by comparison with the experimental results. The masonry in the integral model, as-simulated by the same unit, is a composite homogeneous material with the characteristics of both block and mortar. The behavior of the mortar is not considered separately. The reinforcement is distributed in the wall according to the actual strength, diameter, and position of the model.

The three-dimensional (3D) finite element model established in this study has two types of elements. The 3D linear reduction integral element (C3D8R) [23,24] was adopted for the masonry, core concrete, and top beam. The steel bar is a slender material and its shear resistance is weak under actual working conditions, so the shearing effect was neglected in the model; the steel bar was simplified into a 3D truss element with two degrees of freedom, T3D2. This model does not consider the bond slip between steel and concrete. The connection between steel and concrete is represented by embedding technology. The element embedding technique places slave elements into another group of main elements to constrain the translational freedom of the embedded slave element nodes. A binding constraint was also adopted between the masonry and the top beam. A vertical compressive stress of 0.35 MPa was applied to the top beam and the bottom surface of the masonry was completely fixed. The same cyclic load was applied to the reference point coupled with the right surface of top beam as the test loading system.

A bilinear ideal elastic-plastic model was adopted for the reinforcements. The plastic damage model in ABAQUS was used for the

masonry and grouted concrete. For the masonry wall, the compression constitutive relation was adopted as given in Equations (2-1) [25]; the tensile constitutive relation was taken according to the Chinese Code for Design of Concrete Structures (GB 50010–2010). The elastic modulus in compression was considered the same as that in tension. The masonry elastic modulus values are shown in Equations (2-2) [26]. The constitutive relation recommended by the Chinese Code for Design of Concrete Structures (GB 50010–2010) was used for grouted concrete. The main material parameters are listed in Tables 3 and 4.

$$\begin{cases} \frac{\sigma}{f_m} = 1.15\left(\frac{\varepsilon}{\varepsilon_0}\right) - 0.15\left(\frac{\varepsilon}{\varepsilon_0}\right)^2, & 0 \leq \frac{\varepsilon}{\varepsilon_0} \leq 1 \\ \frac{\sigma}{f_m} = 1.6 - 0.6\left(\frac{\varepsilon}{\varepsilon_0}\right), & 1 \leq \frac{\varepsilon}{\varepsilon_0} \leq 4 \end{cases}, \rightarrow \varepsilon_0 = 0.0023 \quad (2-1)$$

$$E = \frac{1.15}{\varepsilon_0} f_m, \quad \varepsilon_0 = 0.0023 \quad (2-2)$$

3.2. Model verification

3.2.1. Force-displacement curves

Fig. 12 shows a comparison between the simulated and test-based load-displacement curves of specimens. The calculated results are shown in Table 5. As shown in Tables 2 and 5, the curves obtained by finite element analysis deviate somewhat from the measured load-displacement curves but the overall trends are consistent. The main reason for the deviation is that after entering the elastoplastic stage, the finite element analysis does not consider the damage caused by cracks opening and closing under cyclic loading. The simulated load-displacement curve drops more steeply and with obvious symmetry in the two loading directions while the test values agree well with the

Table 7
Simulation results.

Specimen number	Crack		Peak		Failure		K_e /kN.mm ⁻¹	μ
	P_{cr} /kN	Δ_{cr} /mm	P_{max} /kN	Δ_{max} /mm	P_u /kN	Δ_u /mm		
PW	58.35	0.51	107.33	1.13	91.23	1.41	114.41	2.76
ZW-1	92.12	0.57	175.12	1.70	148.85	2.73	161.61	4.79
ZW-2	95.44	0.67	168.35	2.11	142.56	2.53	141.79	3.78
ZW-3	65.64	0.54	154.01	1.99	130.91	1.99	121.56	3.68
ZW-4	121.76	0.87	196.76	2.62	173.09	4.92	139.95	5.66
XCW-1	114.65	0.80	192.48	2.39	167.25	3.11	143.32	3.89

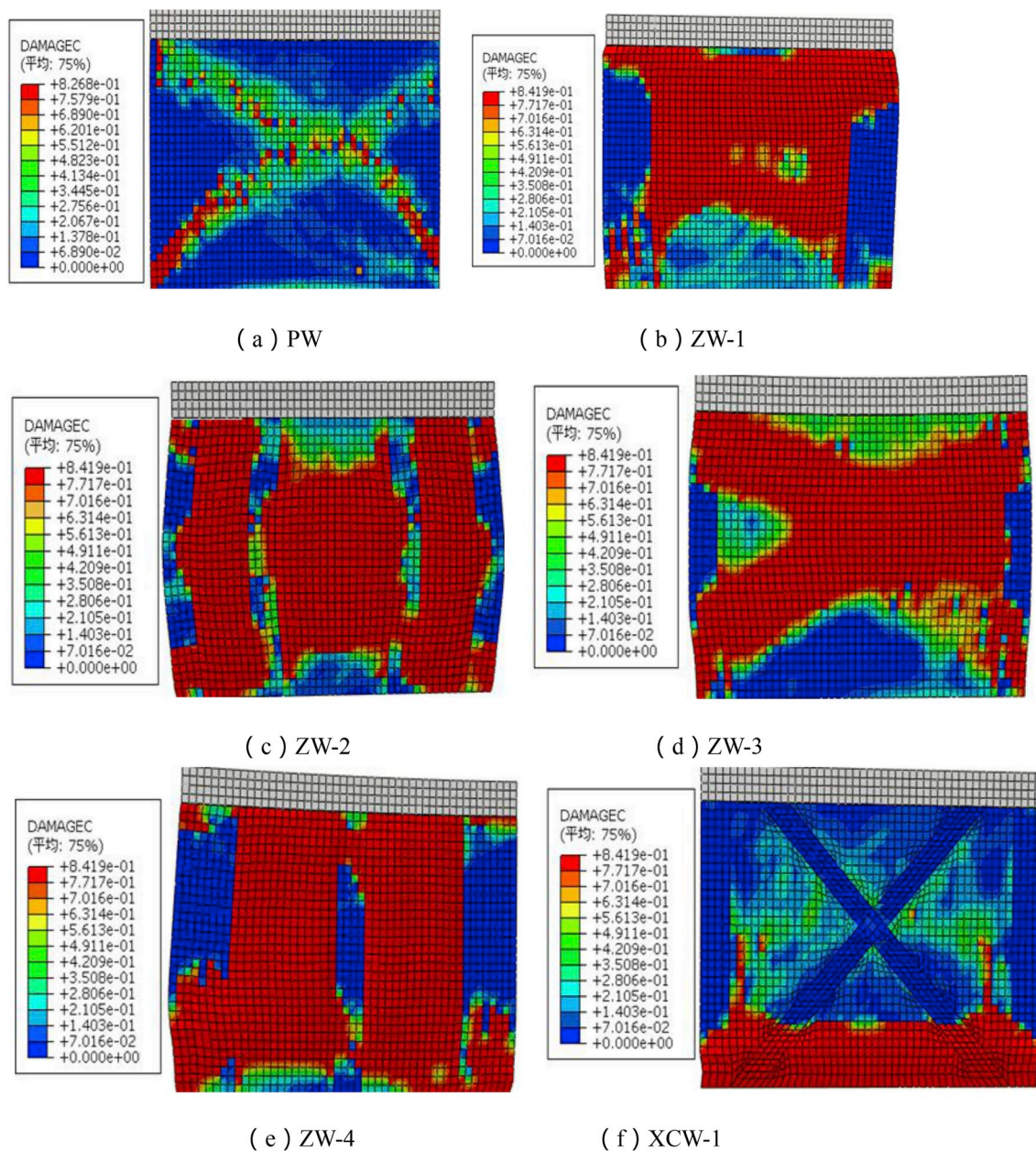


Fig. 18. Final compression damage distributions.

simulated values only in a single loading direction. The horizontal steel tie mesh in the wall was not included in the finite element analysis, so the calculated peak load of specimen ZW-2 was smaller than the test value. The tests and simulations both indicate that the built-in structural column, core column, and diagonal brace can significantly improve the bearing capacity, initial stiffness, and displacement ductility of the wall structure. Different structural measures exert different improvement effects on masonry-related properties.

3.2.2. Compression damage distribution

The final compression damage distribution from the simulations and failure modes from tests of each specimen are shown in Fig. 13. There were no specialized structural measures in specimen PW and the final distribution of its compression damage is X-shaped. X-shaped damage occurred first in the masonry part of specimen ZW-1 (built-in structural column and core column in a concentrated layout scheme), and then developed along the main crack into the ends of the structural column and core column as the load increased. In specimen ZW-2 (built-in

structural column and core column in a dispersed layout scheme), damage first appeared in the masonry between the built-in structural column and core column then expanded along the main crack of the wall into the ends of the built-in structural column and core column as the load increased. The final compression damage in specimen XCW-1 was concentrated at the bottom of the wall including the root of the diagonal brace and the built-in structural column. The compression damage distributions of the specimens obtained by finite element simulation are basically consistent with the damage modes of the walls observed during the test.

3.2.3. Stiffness degradation curves

A comparison between the stiffness degradation curves of each specimen obtained by finite element analysis and experimental tests is shown in Fig. 14. The inherent defects of the material itself during the test and the neglect of material damage under cyclic loading during the finite element simulation created some deviation between the finite element analysis and measured wall stiffness degradation curve, but the

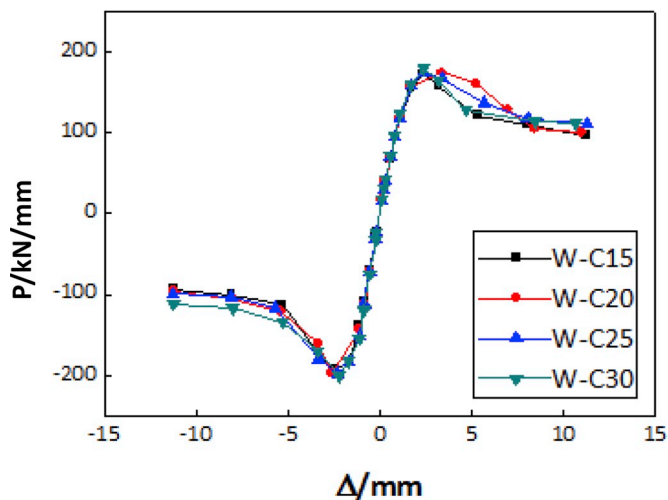


Fig. 19. Load-displacement curves.

trends are consistent. After entering the elastoplastic stage, the idealization of finite element analysis drove stiffness near the peak point above the measured stiffness. When the wall with the built-in structural scheme entered the failure stage at a critical point in the loading process, the stiffness degradation curve of the finite element simulation was basically coincident with that obtained in the experiment; both gradually form a horizontal straight line. The hollow block somewhat enhances the initial stiffness of the structure and the stiffness degradation slows down in the later loading stages. The stiffness of ZW-1 degraded slowly, indicating that the built-in structural and core columns have better restraining and deformation-resistance effects on the wall when they are placed in a concentrated layout at the ends of the wall.

3.3. Finite element analysis of walls with different structural measures

The finite element method proposed in this paper is reliable for all wall specimens tested. Two additional finite models, ZW-3 and ZW-4 (Table 6, Fig. 15), were built to analyze the seismic performance of the wall with different built-in structural measures to determine the optimal construction scheme.

3.4. Load-displacement skeleton curves

The simulated load-displacement skeleton curves of all walls are shown in Fig. 16 and the calculated values are shown in Table 7.

As shown in Table 7 and Fig. 16, the hollow-block wall with a built-in structural scheme shows significantly improved bearing capacity, equivalent initial stiffness, and displacement ductility over other specimens. The bearing capacity of specimens ZW-4 and XCW-1 increased the most followed by specimens ZW-1 and ZW-2; specimen ZW3 showed the minimum increase in bearing capacity among them. The concentrated built-in structural column and core column layout at the wall ends, or an appropriate addition of the core column in the middle

Table 8 Simulation results.

Specimen number	Crack		Peak		Failure		$K_e/kN.mm^{-1}$	μ
	P_{cr}/kN	Δ_{cr}/mm	P_{max}/kN	Δ_{max}/mm	P_0/kN	Δ_u/mm		
W-C15	110.98	0.85	192.92	2.55	163.98	4.02	130.56	4.73
W-C20	121.76	0.87	196.76	2.62	167.25	4.92	139.95	5.66
W-C25	135.13	0.91	197.73	2.28	168.07	3.84	148.49	4.22
W-C30	142.51	0.97	200.96	2.22	170.82	3.30	146.91	3.40

of the wall, is most effective in improving the bearing capacity of the wall. In terms of equivalent initial stiffness, specimen ZW-1 increased the most followed by ZW-2, ZW-4, XCW-1, and finally specimen ZW-3. The centralized layout of the built-in structural and core columns at two ends of the wall is optimal in terms of equivalent initial stiffness. Specimen ZW-4 showed the greatest improvement in displacement ductility followed by specimens ZW-1. ZW-2, ZW3, and XCW-1, which all improved to roughly the same extent and only slightly. The concentrated built-in structural and core column layout at two ends of the wall, or a core column added in the middle of the wall, is optimal for improving the displacement ductility of the wall.

3.5. Stiffness degradation curves

The secant stiffness degradation curve of each wall is shown in Fig. 17. It appears that the initial stiffness of the hollow-block wall with any built-in structural scheme is improved to a certain extent over that of PW. Specimens ZW-2, ZW-4, and XCW-1 show the most significant improvement. The stiffness of specimen PW drops rapidly upon the application of cyclic loads while the other five specimens show varying degrees of stiffness degradation (larger than that of PW) before macroscopic cracks appear. The decrease is greater when the initial stiffness is greater. The stiffness tends to degrade very slowly after the specimen reaches its ultimate bearing capacity.

3.6. Compression damage distribution

The final compression damage distributions of specimens ZW-3 and ZW-4 are shown in Fig. 18.

As shown in Fig. 18, the final compression damage distribution of specimen ZW-3 is X-shaped, similar to PW but with larger damage areas. This may be because specimen ZW-3 only has a wall-end structural column, which creates less constraint on the wall. Specimens ZW-1 and ZW-2 have an additional core column at the end and the middle of the wall, respectively, so the restraining effect on the wall is increased; damage first appeared in the masonry part and then expanded as the load increased until, ultimately, the end of the built-in structural column and core column were damaged along the oblique direction of the masonry. The damage process of specimen ZW-4 is basically consistent with those of ZW-1 and ZW-2 as per the combination of the structural characteristics of both ZW-1 and ZW-2, but the damage distribution area and energy-consuming area were larger and more uniform.

Built-in structural columns and core columns concentrated on the ends of the wall have stronger restraining effect on the intermediate wall, and reinforced concrete has higher energy dissipation capacity than masonry. ZW-1 and ZW-4, and especially ZW-4, have a larger damage area, higher energy consumption capacity, and better overall seismic performance than other specimens.

4. Influence of grouted concrete strength on seismic performance of wall

Four finite element models of the wall were established based on the optimal structural scheme ZW-4 with the same hollow-block strength

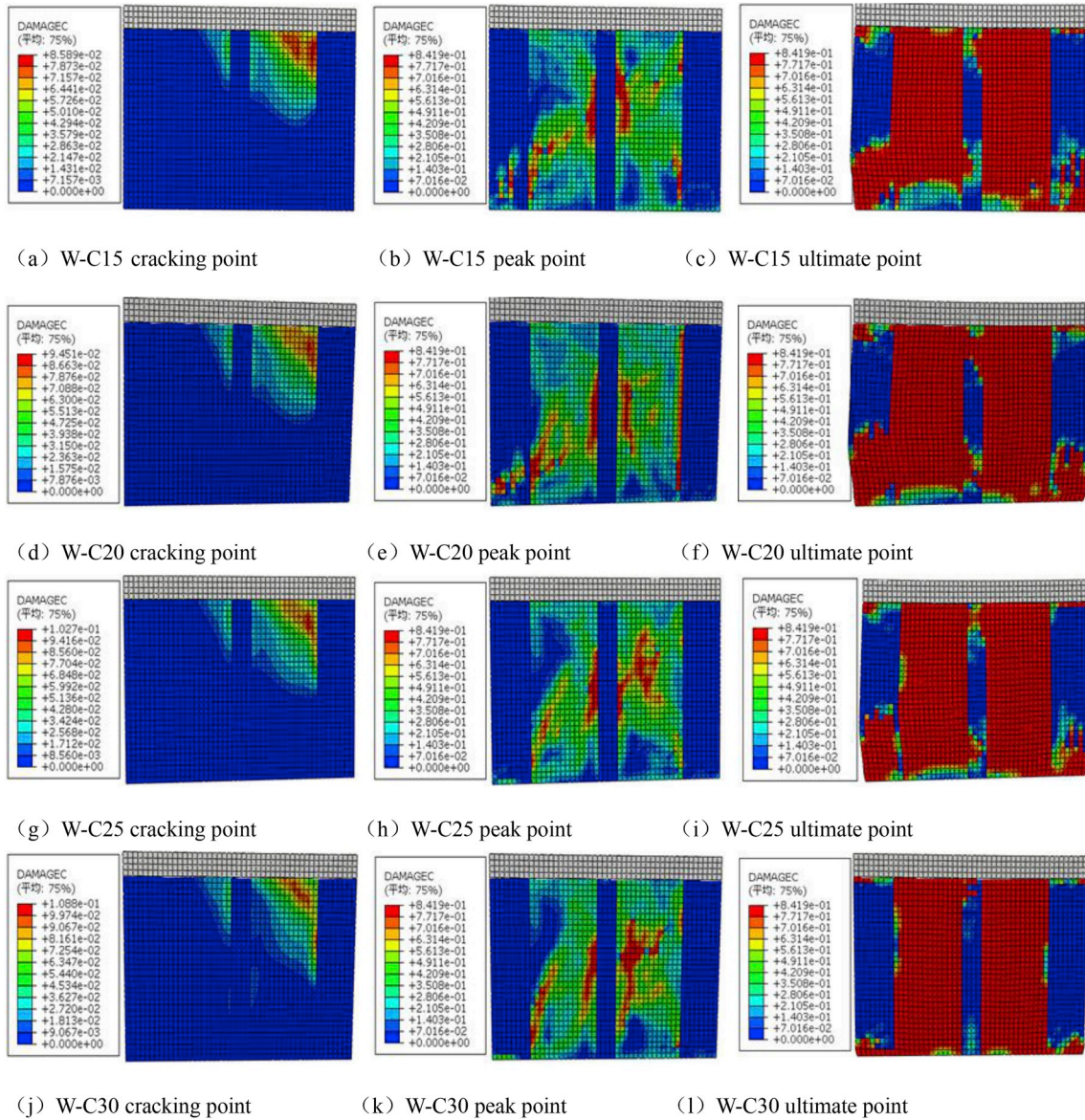


Fig. 20. Compression damage distribution.

but different concrete grades, C15, C20, C25, and C30. The model numbers are W-C15, W-C20, W-C25, and W-C30. The main goal of this analysis was to determine the effects of grouted concrete strength on the seismic performance of reinforced hollow-block masonry structures.

4.1. Load-displacement skeleton curves

The load-displacement skeleton curves are shown in Fig. 19. As shown in Table 8 and Fig. 19, the cracking load, peak load, and failure load of the wall all improved as the grouted concrete strength increased. The cracking load improved to the greatest extent among them. Compared to specimen W-C15, the cracking loads of specimens W-C20, W-C25, and W-C30 increased by 9.71%, 21.76%, and 28.41%, respectively. The peak load and failure load increased by 1.99%, 2.49%, and 4.17%, respectively. The equivalent initial stiffness of each wall also increased as the grouted concrete strength increased; among them, that of W-C25 increased the most. Compared to specimen W-C15, the equivalent initial stiffness of specimens W-C20, W-C25, and W-C30 increased by 7.19%, 13.73%, and 12.52%, respectively. The displacement ductility of the wall was maximal with grouted concrete strength of C20.

4.2. Compression damage distribution

The compression damage distributions of the walls are shown in Fig. 20.

As shown in Fig. 20, the damage area at the point of cracking decreased but the damage severity increased as concrete strength increased. At the peak point, the entire masonry part was damaged with a severe damage area that increased as grouted concrete strength increased. The intermediate part of each specimen was seriously damaged at the moment of failure. The ends of the structural column and core column were also seriously damaged along the diagonal direction of the wall. The extent of damage to the structural and core columns decreased as the grouted concrete strength increased. There was a larger damage area in the walls of W-C20 and W-C25, which suggests that these walls have higher energy consumption than others.

5. Conclusion

Horizontal cyclic loading tests and nonlinear finite element analysis were conducted in this study to observe the effects of different built-in structural schemes and grouted concrete strength on the seismic

performance of PGM-BB specimens. The conclusions can be summarized as follows.

- (1) Compared with normal masonry walls, walls with built-in structural configuration are more efficient and cost-effective because no formwork or large construction equipment are needed.
- (2) When the built-in structural column and core column are in a concentrated layout at two ends of the wall, the bearing capacity, equivalent initial stiffness, and displacement ductility of the wall are markedly enhanced compared to the normal scheme. A built-in structural column and core column in a dispersed layout exert a uniform constraint on the wall which benefits its overall working performance. A horizontal steel tie mesh between the structural column and core column effectively bonds them resulting in a strong restraining effect which further enhances the bearing capacity, ductility, and energy consumption of the walls.
- (3) The built-in diagonal brace greatly improves the bearing capacity and stiffness of the wall but does not significantly improve its ductility.
- (4) The optimal design scheme includes built-in structural columns placed at two ends of the wall and core columns placed not only at the two ends but also at the middle. A horizontal steel tie mesh should also be used to ensure effective bonding among the columns. The appropriate grouted concrete strength for the MU7.5 hollow block is C20 or C25.

Conflicts of interest

The authors declare no conflicts of interest regarding the publication of this paper.

Data availability

The data used to support the findings of this study are included within the article.

Acknowledgments

The research described in this paper was financially supported by the National Natural Science Foundation of China under Grant Nos. 51678389 and 51508374.

References

- [1] Yu J, Zhang F, Bai G. Experimental study on shear behaviour of recycled concrete hollow block masonry. *Mater Res Innov* 2015;19(S8):579–83.
- [2] Hago AW, Hassan HF, Rawas AA, et al. Characterization of concrete blocks containing petroleum-contaminated soils. *Constr Build Mater* 2007;21(5):952–7.

- [3] Dhanasekar M, Thamboo JA, Nazir S. On the in-plane shear response of the high bond strength concrete masonry walls. *Mater Struct* 2017;50(5):214.
- [4] Ömer Can, “Investigation of seismic performance of in-plane aligned masonry panels strengthened with Carbon Fiber Reinforced Polymer”. *Constr Build Mater* 2018;186(20):854–62.
- [5] Reboul N, Larbi AS, Ferrier E. Two-way bending behaviour of hollow concrete block masonry walls reinforced by composite materials. *Compos B Eng* 2018;137(15):163–77.
- [6] Popehn JRB, Schultz AE, Drake CR. Behavior of slender, posttensioned masonry walls under transverse loading. *J Struct Eng* 2007;133(11):1541–50.
- [7] Yu P, Silva P, Nanni A. In-plane performance of unreinforced concrete masonry strengthened with prestressed GFRP Bars. *J Compos Constr* 2017. [https://doi.org/10.1061/\(ASCE\)CC.1943-5614.0000717](https://doi.org/10.1061/(ASCE)CC.1943-5614.0000717).
- [8] Adolfo P, Alejandro RG, Nayar G, et al. Nonlinear earthquake capacity of slender old masonry structures prestressed with steel, FRP and NiTi SMA tendons. *Steel Compos Struct* 2018;26(2):213–26.
- [9] Giaretton M, Dizhur D, Garbin E, Ingham JM, Porto F. In-plane strengthening of clay brick and block masonry walls using textile-reinforced mortar. *J Compos Constr* 2018. [https://doi.org/10.1061/\(ASCE\)CC.1943-5614.0000866](https://doi.org/10.1061/(ASCE)CC.1943-5614.0000866).
- [10] Kouris LAS, Triantafillou TC. State-of-the-art on strengthening of masonry structures with textile reinforced mortar. *Constr Build Mater* 2018;188(10):1221–33.
- [11] Farooq SH, Shahid I, Ilyas M. Seismic performance of masonry strengthened with steel strips. *KSCE J Civil Eng* 2014;18(7):2170–80.
- [12] Tang D, Ding D. Regional report: Far east: Concrete block masonry development in China. *Concr Eng Int* 2006;10(4):50–1.
- [13] Dhanasekar M, Haider W. Effect of spacing of reinforcement on the behaviour of partially grouted masonry shear walls. *Adv Struct Eng* 2011;14(2):281–93.
- [14] Janaraj T, Dhanasekar M. Effectiveness of two forms of grouted reinforced confinement methods to hollow concrete masonry panels. *J Mater Civ Eng* 2015. [https://doi.org/10.1061/\(ASCE\)MT.1943-5533.0001295](https://doi.org/10.1061/(ASCE)MT.1943-5533.0001295).
- [15] Sarma BS, Sreenath HG, Bhagavan NG, Ramachandra MA, Vimalanandam V. Experimental studies on in-plane ductility of confined masonry panels. *ACI Struct J* 2003;100(3):330–6.
- [16] Singhal V, Rai DC. Behavior of confined masonry walls with openings under in-plane and out-of-plane loads. *Earthq Spectra* 2018;34(2):817–41.
- [17] Belghiat C, Messabhia A, Plassiard JP, et al. Experimental study of double-panel confined masonry walls under lateral loading vol 20. 2018. p. 531–43.
- [18] Banting Bennett R, El-Dakhkhni Wael W. Force and displacement-based seismic performance parameters for reinforced masonry structural walls with boundary elements. *J Struct Eng* 2012;138(12):1477–91.
- [19] Mohamed Ezzeldin, El-Dakhkhni Wael, Wiebe Lydell. Experimental assessment of the system-level seismic performance of an asymmetrical reinforced concrete block-wall building with boundary elements. *J Struct Eng* 2017. [https://doi.org/10.1061/\(ASCE\)ST.1943-541X.0001790](https://doi.org/10.1061/(ASCE)ST.1943-541X.0001790).
- [20] Zhou Z, Cao W, Dong H, Zhang J. Experimental study on seismic performance of new concrete block masonry wall with constructional columns. *J Earthquake Eng Eng Vib* 2012;32(3):86–91. [in Chinese].
- [21] Noor-E-Khuda S, Dhanasekar M. Masonry walls under combined in-plane and out-of-plane loadings. *J Struct Eng* 2018;144(2):04017186.
- [22] Ala T Obaidat, Ahmad Abo El Ezz, Khaled Galal. Compression behavior of confined concrete masonry boundary elements”. *Eng Struct* 2017;132:562–75.
- [23] Nascimbene R. “Towards non-standard numerical modeling of thin-shell structures: geometrically linear formulation”. *Int J Comput Methods Eng Sci Mech* 2014;15(2):126–41.
- [24] Belytschko T, Wong BL, Chiang H-Y. Advances in one-point quadrature shell elements. *Comput Methods Appl Mech Eng* 1992;96(1):93–107.
- [25] Liu G. “The research on the basic mechanical behavior of masonry structure” [D]. Changsha: Hunan University; 2005. [in Chinese].
- [26] Liu G, Shi C, Liu Y. Analyses of the elastic modulus values of masonry. *J Hunan Univ (Nat Sci)* 2008;4:29–32.